Geophysical Research Letters

RESEARCH LETTER
10.1029/2019GL082114

This article is a companion to Ojha et al. (2019), https://doi.org.10.1029/2019gl082294.

Key Points:
- We constrain the composition of the cavi unit at two locations beneath the north polar layered deposits on Mars using SHARAD observations
- The cavi unit contains more than 50% water ice by volume and is organized in alternating layers of water ice and aeolian sand
- The cavi unit is one of the largest water reservoirs on Mars and its layers record the growth and retreat of ancient polar caps

Supporting Information:
- Supporting Information S1
- Data Set S1
- Data Set S2

Correspondence to:
S. Nerozzi,
stefano.nerozzi@utexas.edu

Citation:
Nerozzi, S., & Holt, J. W. (2019). Buried ice and sand caps at the north pole of Mars: Revealing a record of climate change in the cavi unit with SHARAD. *Geophysical Research Letters*, *46*, 7278–7286. https://doi.org/10.1029/2019GL082114

Received 23 JAN 2019
Accepted 29 APR 2019
Accepted article online 22 MAY 2019
Published online 8 JUL 2019

Buried Ice and Sand Caps at the North Pole of Mars: Revealing a Record of Climate Change in the Cavi Unit With SHARAD

S. Nerozzi[1] **and J. W. Holt**[2]

[1]Institute for Geophysics, Jackson School of Geosciences, The University of Texas at Austin, Austin, TX, USA, [2]Lunar and Planetary Laboratory, Department of Planetary Sciences, University of Arizona, Tucson, AZ, USA

Abstract The cavi unit at the north pole of Mars is a deposit of aeolian sand and water ice underlying the Late Amazonian north polar layered deposits. Its strata of Middle to Late Amazonian age record wind patterns and past climate. The Mars Reconnaissance Orbiter Shallow Radar (SHARAD) reveals extensive internal and basal layering within the cavi unit, allowing us to determine its general structure and relative permittivity. Assuming a basalt composition for the sand ($\varepsilon' = 8.8$), results indicate that cavi contains an average ice fraction between 62% in Olympia Planum and 88% in its northern reaches beneath the north polar layered deposits and thus represents one of the largest water reservoirs on the planet. Internal reflectors indicate vertical variability in composition, likely in the form of alternating ice and sand layers. The ice layers may be remnants of former polar caps and thus represent a unique record of climate cycles predating the north polar layered deposits.

Plain Language Summary The north polar region of Mars includes the so-called cavi unit, a deposit of water ice and sand hundreds of million years old that lies beneath the current ice cap. The Shallow Radar on Mars Reconnaissance Orbiter can image through the cavi unit deposits, revealing their internal structure and composition. We find that these deposits are very rich in ice, which lies in horizontal slabs alternated with sand. The occurrence and volume of ice slabs increase toward the north pole. This ice may be the leftover of former ice caps that diminished during warm periods and therefore represent an important record of past Martian climate. The large volume of ice preserved within the cavi unit represents one of the largest water reservoirs on the planet.

1. Introduction

The cavi unit is an aeolian deposit comprising a large fraction of Planum Boreum in the northern hemisphere of Mars. Cavi and the older rupēs unit together make up the so-called basal unit (BU; Fishbaugh & Head, 2005) that lies beneath the north polar layered deposits (NPLD; Figure 1a). Cavi accumulation began in the Middle Amazonian, recording wind patterns and climate conditions and transitions from hundreds of mega-anna through the initial emplacement of the NPLD, as indicated by a gradational and transgressive stratigraphic upper contact (Brothers et al., 2018; Nerozzi & Holt, 2018; Skinner & Herkenhoff, 2012; Tanaka et al., 2008; Tanaka & Fortezzo, 2012). Analysis of radar sounding profiles, visible outcrop imagery, and spectrometry has determined that cavi is composed of a mixture of sand-sized lithic materials organized in aeolian cross strata and dune forms weakly cemented by water ice and interbedded with purer ice layers (e.g., Byrne & Murray, 2002; Fishbaugh & Head, 2005; Phillips et al., 2008; Selvans et al., 2010; Tanaka et al., 2008). However, among these numerous studies, there is no consensus on the precise composition and large-scale internal structure of cavi, and it has remained unclear which fraction, water ice or sand, dominates.

Cavi locally overlies either the Vastitas Borealis interior unit (VBIU) or the rupēs unit and is separated from the latter by a large erosional unconformity with hundreds of meters of relief (Tanaka et al., 2008; Tanaka & Fortezzo, 2012). Cavi is mostly buried underneath the NPLD in Planum Boreum (Brothers et al., 2015) and is thought to make up most of the volume of Olympia Planum underneath the sand sea of Olympia Undae (Byrne & Murray, 2002; Ewing et al., 2010; Fishbaugh & Head, 2005; Tanaka & Fortezzo, 2012; Zuber et al., 1998). Radar profiles obtained from the Mars Advanced Radar for Subsurface and Ionosphere Sounding and the Shallow Radar (SHARAD) provide further evidence of the continuity of the BU underneath Olympia Planum (Phillips et al., 2008; Selvans et al., 2010). Cavi is exposed only along a few arcuate

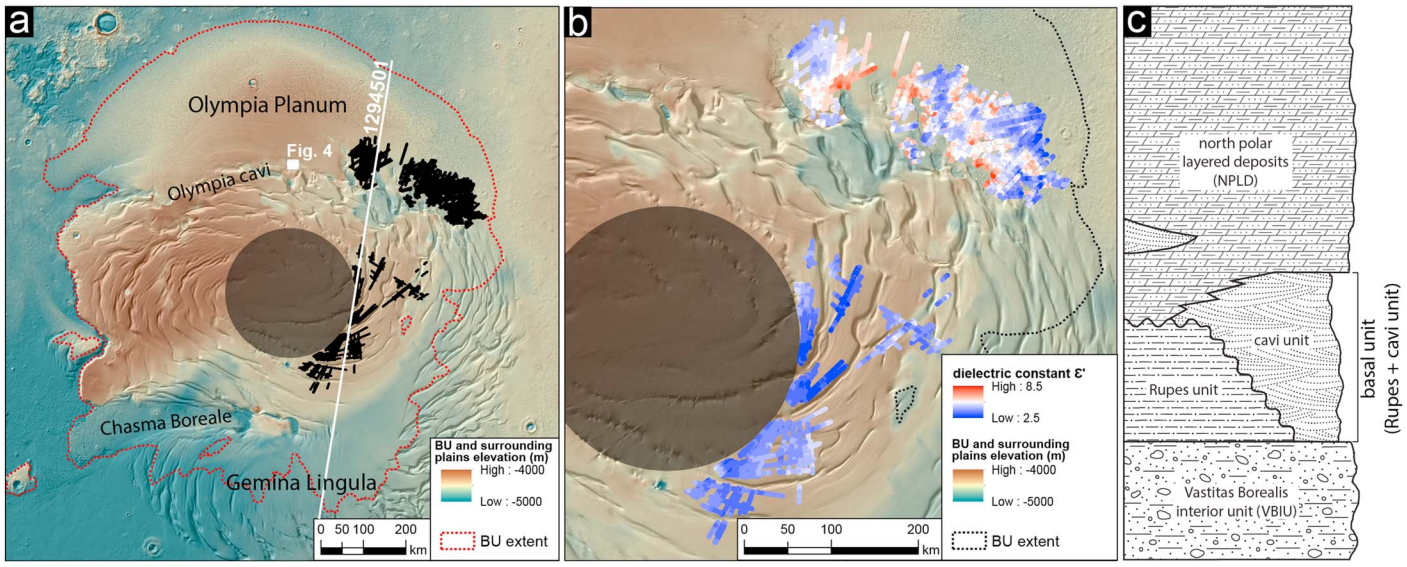

Figure 1. (a) Elevation map of the basal unit (BU) and surrounding plains, with superimposed shaded relief of the modern Planum Boreum topography, and locations of the radar profile in Figure 2, and High Resolution Imaging Science Experiment image in Figure 4. The black points indicate cavi basal detections. (b) Details of calculated relative permittivity of cavi. (c) Schematic representation of the stratigraphic relationships between the Planum Boreum geologic units, modified from Tanaka et al. (2008).

scarps in Chasma Boreale and Olympia cavi (Edgett et al., 2003) and on the floor of some interdune areas of Olympia Undae (Ewing et al., 2010; Tanaka et al., 2008).

Along visible outcrops, cavi is dominated by cross strata and dune forms of low albedo material, interpreted as basalt sand, forming undulated and discontinuous beds alternating with bright, fractured layers of substantial thickness, likely composed of relatively pure water ice (Byrne & Murray, 2002; Edgett et al., 2003; Herkenhoff et al., 2007; Malin & Edgett, 2001). Water ice strata become more frequent and thicker toward the top of cavi, sometimes forming nearly pure ice dunes (Brothers et al., 2015; Brothers et al., 2018). Spectroscopy observations confirm the presence of basalt sand and water ice along cavi exposures and also detect the signature of hydrated minerals (Calvin et al., 2009; Horgan et al., 2009), identified conclusively as gypsum (Massé et al., 2010, 2012). Gypsum was found in large quantities (up to 35% by volume) across Olympia Undae (Fishbaugh et al., 2007; Langevin et al., 2005) and in minor quantities in the circumpolar dune fields (Calvin et al., 2009; Horgan et al., 2009). The major gypsum source has been identified in the eroding exposures of cavi (Calvin et al., 2009; Massé et al., 2010, 2012; Roach et al., 2007).

The bulk composition of cavi (and the BU in general) has been difficult to determine, mostly due to the lack of visible exposures. Orbital sounding radars can penetrate through the NPLD and the BU to reveal their compositions. Selvans et al. (2010) observed that, in general, the strength of Mars Advanced Radar for Subsurface and Ionosphere Sounding echo from the base of the BU is consistent with low attenuation in the BU, suggesting that the unit contains only a few percent impurities mixed with water ice; however, some regions lacked or had weak basal returns, indicating stronger attenuation or scattering of the radar signal. SHARAD can penetrate through the NPLD to reveal the surface of the BU in high detail (Brothers et al., 2015; Nerozzi & Holt, 2017; Phillips et al., 2008; Putzig et al., 2009). Lauro et al. (2012) used SHARAD reflectivity of the NPLD/cavi interface in Boreales Scopuli to determine a relative permittivity distribution for cavi with values of $\varepsilon' = 5$–6, compatible with a roughly equal mixture of basalt and water ice for the uppermost surface of the unit.

SHARAD appears unable to penetrate the surface of the rupēs unit (Brothers et al., 2015; Phillips et al., 2008) but can image through cavi at several locations, revealing internal reflectors and its basal contact with the VBIU (Phillips et al., 2008; Figure 2). We use this basal detection to calculate the bulk relative permittivity of cavi and, in turn, constrain its composition and water ice content. Furthermore, the internal reflectors allow us to reconstruct the general stratigraphic architecture of the unit and understand how it evolved through the Middle and Late Amazonian under changing global climate.

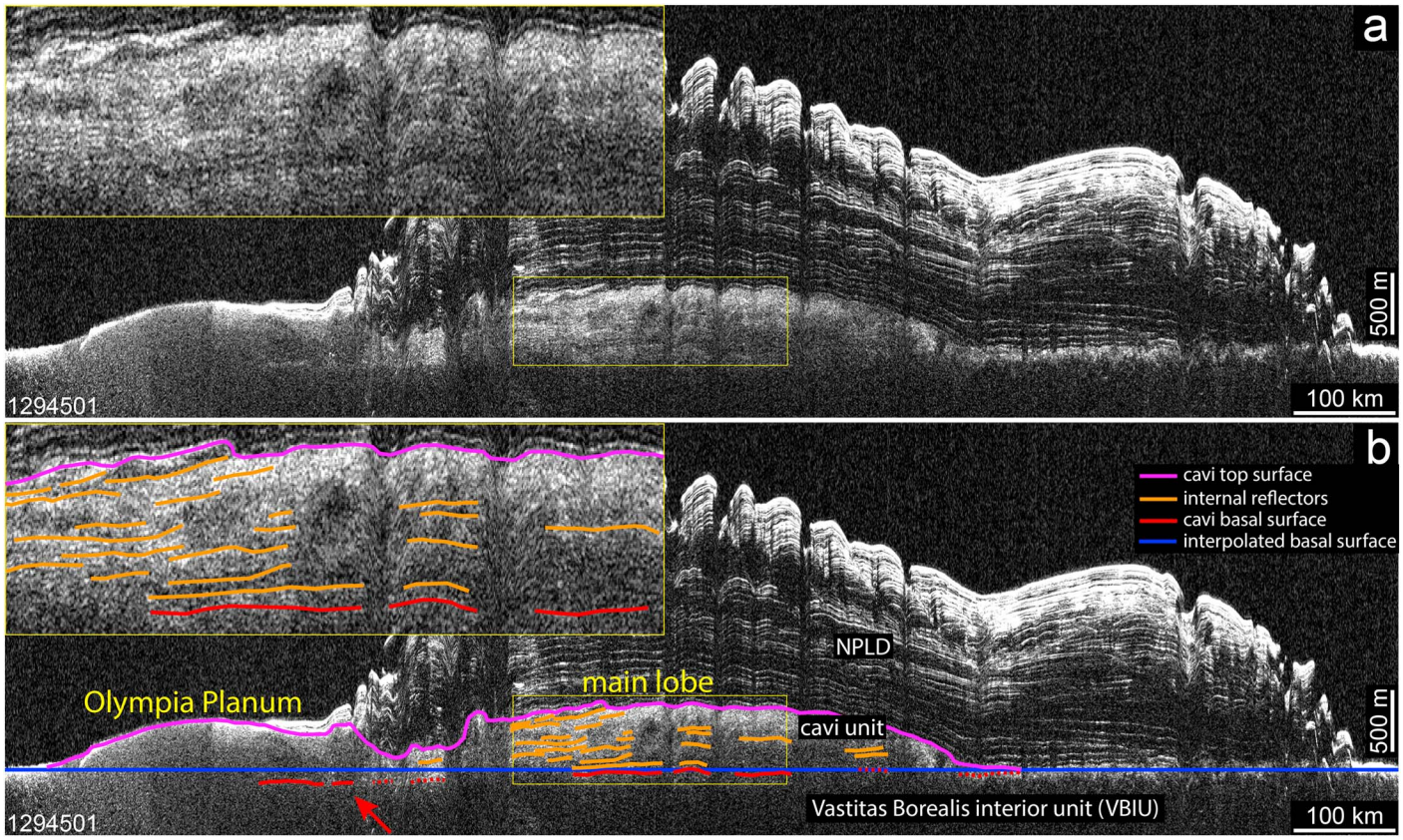

Figure 2. (a) Original and (b) interpreted Shallow Radar profile showing basal and internal reflectors within cavi. The profile is depth corrected assuming a bulk composition of water ice ($\varepsilon' = 3.1$). Note the characteristic diffuse radar return of the cavi unit, which is typical of dune fields, such as the one in Olympia Planum (Olympia Undae). The cavi basal reflector in Olympia Planum is below the interpolated basal surface (red arrow), indicating a relative permittivity higher than that of water ice. NPLD = north polar layered deposits.

2. Data and Methods

SHARAD is an orbital sounding radar spanning 15–25 MHz with a linear frequency modulation, allowing a vertical resolution of ~15 m in free space and ~8.4 m in water ice after pulse compression (Seu et al., 2004, 2007). The horizontal ground resolution after processing is 0.3–1 km along-track and 3–6 km across-track (Seu et al., 2007). We use the US SHARAD products from the NASA Planetary Data System (PDS) Geosciences node, generated by a processing routine performing aperture focusing and implementing an autofocus ionospheric correction (Campbell et al., 2011). The comprehensive and dense coverage of Planum Boreum with over 3,000 profiles allows us to collect a large number of cavi measurements.

We calculate the relative permittivity of each cavi unit observation as follows:

$$\varepsilon_c^{'} = \left(\frac{ct}{2h}\right)^2 \quad (1)$$

where t is the two-way time delay between the cavi top and basal surfaces, c is the speed of light in vacuum, and h is the thickness of the unit. We determined the two-way time delay by mapping the cavi top and basal surface reflectors within 129 SHARAD profiles in the Halliburton's DecisionSpace interpretation suite (Figure 1). This software implements a semi-automatic tracing algorithm that helps the interpreter in picking the peak power of a specific reflector with consistency and can connect profiles at their intersections, thus allowing the tracing of a continuous reflector around areas with off-nadir reflections (i.e., "clutter") and/or poor quality of radar returns. We determined the elevation of the upper surface of cavi by removing the thickness of the overlying NPLD where present, assuming a bulk composition of water ice ($\varepsilon' = 3.1$; Grima et al., 2009). For the cavi basal surface, we only picked reflectors that connected laterally with the

exposed VBIU surface, because in our study areas the cavi base corresponds to the surface topography of the VBIU. The VBIU appears "relatively featureless" and "remarkably flat" underneath Planum Boreum (Selvans et al., 2010) and is not deflected under the load of polar deposits (Phillips et al., 2008; Putzig et al., 2009; Selvans et al., 2010). Therefore, we can extrapolate cavi basal topography to determine its absolute elevation by interpolating the Mars Orbiter Laser Altimeter shot points and SHARAD-derived elevations of the surrounding VBIU plains with a sixth degree polynomial. We provide a detailed error estimate in supporting information S1.

We then translated the bulk relative permittivity $\varepsilon'_{\text{cavi}}$ to composition assuming a three-component mixture of basalt ($\varepsilon'_{\text{basalt}} = 8.8$; Nunes & Phillips, 2006), gypsum ($\varepsilon'_{\text{gypsum}} = 6.6$; derived from Heggy et al., 2001; see supporting information S3), and water ice ($\varepsilon'_{\text{ice}} = 3.1$; Brouet et al., 2016; Heggy et al., 2008; Mattei et al., 2014). These correspond to the three major components detected within cavi by previous studies, as discussed above. In order to facilitate interpretations, we constructed a ternary diagram based on the following mixing power law:

$$\varepsilon'^{1/\gamma}_{\text{cavi}} = \phi_{\text{basalt}}\varepsilon'^{1/\gamma}_{\text{basalt}} + \phi_{\text{gypsum}}\varepsilon'^{1/\gamma}_{\text{gypsum}} + \phi_{\text{ice}}\varepsilon'^{1/\gamma}_{\text{ice}} \quad (2)$$

where $\gamma = 2.7$ for ice and sand mixtures (Stillman et al., 2010) and ϕ is the fractional volume of each component. Our basic assumptions for this mixture are that water ice occupies the pore space between lithic grains and no air is present. Analysis of thermal infrared and neutron spectrometry measurements indicates that Olympia Undae is best modeled as ice-cemented aeolian deposits buried by a dry sand cover ~10 cm thick (Feldman et al., 2008; Putzig et al., 2014), and the topography of crater ejecta in the region indicates abundant subsurface ice (Zuber et al., 1998). Furthermore, circumpolar sand dunes often appear to be immobilized due to induration by water ice (Bourke et al., 2008; Ewing et al., 2010; Feldman et al., 2008; Schatz et al., 2006), suggesting that most of the pore space of cavi sand dunes is occupied by water ice rather than air. Aeolian sand deposits on Earth have typical porosities of 34–40% (e.g., Beard & Weyl, 1973; Kolbuszewski et al., 1950), although they may reach extremes of 25–50% (e.g., Atkins & Mcbride, 1992; Beard & Weyl, 1973; Dickinson & Ward, 1994; Pye & Tsoar, 1990). Therefore, if the water ice fraction is larger than 50%, excess ice (i.e., exceeding the expected pore space) is likely present within the mixture.

3. Results

Our exercise reveals that the bulk relative permittivity of cavi has substantial spatial variability (Figure 1b), especially between the regions of Olympia Planum and the central main lobe of cavi, with a trend of decreasing values moving toward the pole. The relative permittivity is more variable in Olympia Planum, where the lower thickness of cavi makes our relative permittivity calculations more sensitive to the small-scale roughness of the basal surface.

SHARAD does not detect internal reflectors in Olympia Planum other than the basal surface. The cavi unit in this region has a normally distributed relative permittivity with an average $\varepsilon' = 4.84$ and a $1 - \sigma = 0.89$ (Figure 3a), a value compatible with the findings of Lauro et al. (2012). Excluding gypsum from the mixture, this value translates to a mixture of 62^{+18}_{-16}% water ice and 38^{+16}_{-18}% basalt (Figure 3c), therefore indicating the presence of excess ice. Nevertheless, the sole presence of gypsum in the mixture can only lower the volume of water ice down to ~44%, on the high-end of aeolian sand porosities. Previous studies detected only a weak signature of gypsum within visible cavi outcrops, suggesting that it constitutes only a very small component compared to basalt. Furthermore, relatively pure water ice layers and cross strata pervade all cavi visible outcrops (e.g., Brothers et al., 2018; Tanaka et al., 2008), including those in Olympia Planum, suggesting that excess ice is the norm within cavi rather than the exception.

The average bulk relative permittivity of the cavi main lobe is significantly lower than that of Olympia Planum at $\varepsilon' = 3.59$ with a $1 - \sigma = 0.46$ (Figure 3b). This value converts to a dominant ice fraction of 83^{+16}_{-15}% and 88^{+11}_{-10}% using pure gypsum and basalt sand, respectively (Figure 3c), similar to the conclusions of Selvans et al. (2010) for the entire BU. This far exceeds the maximum aeolian sand porosity of 50%, meaning that excess ice is certainly present in this region. SHARAD also detects several continuous reflectors within the cavi main lobe, extending for tens to hundreds of kilometers and describing a subhorizontal structure (Figure 2). Radar reflectors arise from significant and laterally consistent changes of composition in the

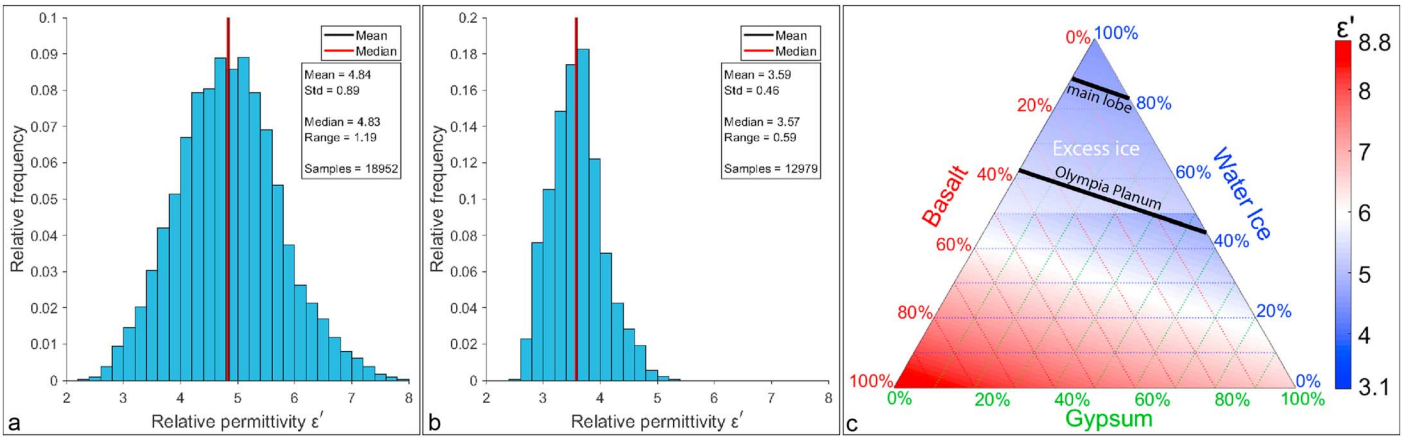

Figure 3. Relative permittivity of cavi in (a) Olympia Planum and (b) main lobe. (c) Average relative permittivity of both study areas plotted on a ternary diagram of calculated permittivity for a mixture of basalt, gypsum, and water ice.

subsurface, thus indicating the presence of extensive layers with varying composition within cavi. The number of reflectors increases at higher latitudes and toward the top of the unit.

4. Discussion

Bulk relative permittivity distributions and the exclusive presence of internal reflectors in the main lobe indicate that cavi has substantial internal heterogeneity. A two-means *t* test performed on the cavi bulk relative permittivity distributions confirms that the mean of the measurements of Olympia Planum is greater than that of the main lobe at the 5 – σ confidence level. The results in Olympia Planum suggest that excess ice is likely present in this region of cavi, which is also ubiquitous in outcrops. Large quantities of gypsum are required to lower the water ice fraction significantly, but previous studies indicate that its abundance is very limited. Moreover, cavi is exposed within the interdune areas of this region (Ewing et al., 2010; Tanaka et al., 2008), meaning that gypsum should have been detected with a strong signature if present in significant concentrations. Instead, gypsum appears to be concentrated along dune crests (Massé et al., 2010). We do not exclude the possibility that a small fraction of air might remain within the pore space, but its presence is not required to explain our results in the context of previous findings. In the cavi main lobe, water ice is by far the dominant fraction, unless a significant volume of air occupies the pore space (>22% assuming basalt as the lithic component). We find this case to be unrealistic given that this region of cavi is buried underneath ~1.5 km of NPLD ice, and we argue that if any air is present in this region, it must be in equal or less amount than in Olympia Planum due to compaction from the overlying ice sheet.

The presence of internal reflectors exclusively within the cavi main lobe gives us insights into its general stratigraphic architecture. Previous investigations suggested that cavi formed by several repeated cycles of aeolian sand migration during warmer periods of high obliquity, alternated with water ice accumulation during colder, low obliquity periods (Brothers et al., 2018; Byrne, 2009; Herkenhoff et al., 2007; Tanaka et al., 2008; Tanaka & Fortezzo, 2012). Our results support the hypothesis of cavi cyclic accumulation of water ice with minor impurities alternated with ice-cemented sand sheets (Figure 4). Sand dunes migrating on top of pure water ice are common in the outskirts of the NPLD (e.g., Massé et al., 2012; Skinner & Herkenhoff, 2012), and partially or completely blanketing over half of the water ice domes within craters surrounding Planum Boreum (Conway et al., 2012). Lowermost NPLD exposures also showcase lithic-rich dunes and layers overlying water ice (Brothers et al., 2018; Tanaka et al., 2008). In this study, we found two sand sheets over 40 km wide and up to 50 m thick overlying NPLD water ice 50 to 100 m thick exposed along Olympia Cavi scarps (Figure 5). These features closely resemble the aeolian deposits of cavi with high-albedo fractured layers and cross strata, suggesting that water ice is likely in excess of pore space even within lithic-rich strata. Due to their thickness and lateral extent, we argue that the ice and sand sheets of Figure 5 are representative of the stratigraphy of the cavi main lobe and create a relative permittivity contrast detected by

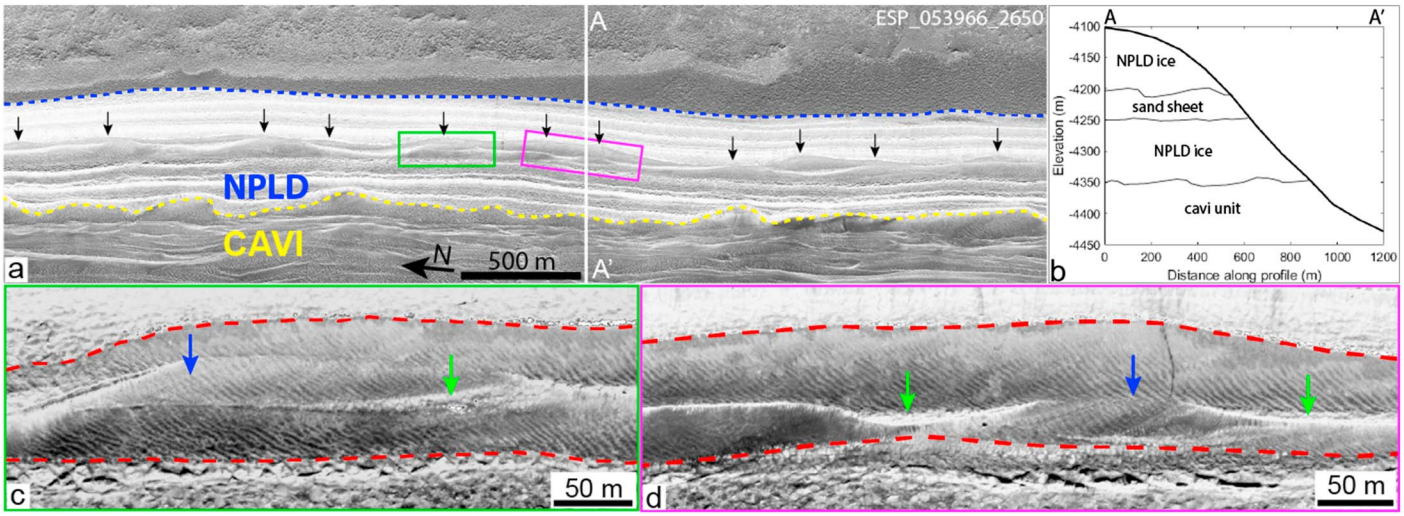

Figure 4. Interpreted structure and composition of cavi along the same profile in Figure 2. We hypothesize that cavi is made of water ice sheets (blue) alternated with sand sheets (orange lines) in the main lobe and becomes richer in lithic components toward the lower latitudes of Olympia Planum. NPLD = north polar layered deposits.

SHARAD as subhorizontal reflectors. Using a linear mixing law and assuming a 50–50% mixture of basalt and water ice for the sand sheets, we find that pure water ice occupies ~76% of the volume of cavi.

Water ice accumulation models predict substantial water ice accumulation during colder periods of low obliquity just before the onset of the NPLD, with the thickest accumulation at high latitudes (Greve et al., 2010; Levrard et al., 2007). For example, Greve et al. (2010) predict the growth of ~500 m of water ice at cavi main lobe latitudes in less than 1 Myr, which is then lost during a period of high spin axis obliquity. However, this model does not include mechanisms that may protect ice from complete sublimation or erosion, such as the burial by sand sheets or the formation of sublimation lags. The process of water ice burial by aeolian deposits was certainly active in the past, as testified by the visible exposure of sand sheets overlying water ice (Figure 5). Cementation by water ice often immobilizes sand dunes (e.g., Schatz et al., 2006), which then become a protective blanket for underlying ice against loss by sublimation and erosion. The sand sheets observed within lowermost NPLD exposures are meters to tens of meters thick and are hence quite capable of preventing ice loss (e.g., Bramson et al., 2017; Chevrier et al., 2007; Skorov et al., 2001; Williams et al., 2008). Another form of protection may come from relatively thin (centimeters to decimeters thick) sublimation lags formed during periods of ice cap instability, perhaps in a form analogous to the desiccated sand layer that blanket the ice-cemented core of Olympia Undae dunes (Feldman et al., 2008; Putzig et al., 2014). Water ice accumulation models are based on orbital solutions that go back to only ~20 Ma before diverging chaotically (Laskar et al., 2004), meaning that several cycles of ice cap growth and burial under

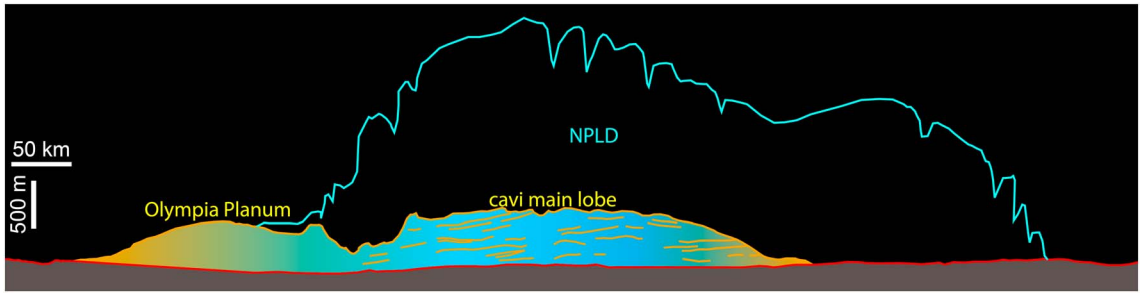

Figure 5. (a) High Resolution Imaging Science Experiment image sample of a steep scarp in Olympia cavi showing a sand sheet ~50 m thick overlying ~100 m of north polar layered deposits (NPLD) water ice (Mars Orbiter Laser Altimeter topographic profile in panel b). Black arrows indicate dune forms. (c, d) Details of the sand sheet showing dune forms, bright cross strata (blue arrows), and fractured layers (green arrows).

sand sheets may have occurred throughout the long history of cavi since the Middle Amazonian. We counted up to 11 superposed reflectors within the cavi main lobe, which may correspond to an equal or higher number of stacked ice and sand sheets (Lalich & Holt, 2016; Nunes & Phillips, 2006). The lack of cavi internal reflectors in the Olympia Planum study area is also interesting and warrants the formulation of two hypotheses. (1) Pure water ice layers are absent within cavi in this region, and thus, there is a lack of relative permittivity contrasts capable of causing radar reflections; alternatively, (2) pure water ice layers exist but are too thin and/or too laterally discontinuous to cause a radar reflection (Lalich & Holt, 2016; Nunes & Phillips, 2006). Modeling of radar reflectivity of thin layers of sand and ice mixtures could provide an effective test of these hypotheses. Nevertheless, both possibilities support our interpretation that less ice is present in cavi outside of the main lobe.

Perhaps the most significant implication of our findings is that cavi not only recorded aeolian and other surface processes in its cross strata and dune forms but also preserved several major water ice accumulation and retreat events. These are likely tied to global climate, date back to the Middle Amazonian, and can be studied with SHARAD, thus opening a new window on an ancient record of global climate changes. Our findings reconcile and confirm the previous findings of Selvans et al. (2010), who argued that the entire BU is very rich in ice, and Lauro et al. (2012), who measured a relative permittivity at the top of cavi compatible with a basaltic sand sheet with 41–59% porosity occupied by water ice. Analysis and inversion of gravity signals over Planum Boreum also indicate that water ice makes up more than 50% of the BU by volume (Ojha et al., 2019). Our results on the relative permittivity of cavi indicate abundant excess ice, making this unit one of the largest water ice reservoirs of the planet after the polar layered deposits. Considering only the study areas, we determine a very conservative minimum cavi volume of 2.1×10^4 km^3 and an ice volume of 1.6×10^4 km^3 or a global equivalent layer of 0.11 m. Expanding this estimate to the entire BU and using a conservative $\varepsilon' = 4.84$, we obtain an ice volume of 2.2×10^5 km^3 (1.53 m global equivalent layer), which falls within the 1.3×10^5 to 3.7×10^5 km^3 volume estimate of Martian midlatitude glacial deposits (Levy et al., 2014). This has important implications on the global water cycle, because cavi gradually trapped large amounts of water ice during its growth.

5. Conclusions

Using a basalt and ice mixture, we find that an ice fraction of 62–88% by volume dominates within the cavi unit, making it one of the largest water ice reservoirs on Mars. The numerous, extensive reflectors within the unit indicate the presence of layers with different compositions, likely in the form of alternating ice and sand sheets. These ice layers may be remnants of former ice caps, protected from complete sublimation during warm periods by aeolian sand blanketing and/or sublimation lags. Therefore, these layers likely represent a unique record of past climate cycles predating the NPLD.

Acknowledgments
This work was supported by the NASA Mars Data Analysis Program grant NNX15AM52G and by the Landmark Software and Services, a Halliburton Company. The data used in this work are available through PDS (https://pds.nasa.gov/). Processed data are attached as supporting information. SHARAD was provided to NASA's Mars Reconnaissance Orbiter mission by the Italian Space Agency (ASI). Ternary plot code is courtesy of Ulrich Theune, University of Alberta. We thank Daniel Lalich and one anonymous reviewer for their constructive contributions to this manuscript.

References

Atkins, J. E., & Mcbride, E. F. (1992). Porosity and packing of Holocene river, dune, and beach sands. *AAPG Bulletin*, *76*(3), 339–355.

Beard, D. C., & Weyl, P. K. (1973). Influence of texture on porosity and permeability of unconsolidated sand. *AAPG Bulletin*, *57*(2), 349–369.

Bourke, M. C., Edgett, K. S., & Cantor, B. A. (2008). Recent aeolian dune change on Mars. *Geomorphology*, *94*(1), 247–255. https://doi.org/10.1016/j.geomorph.2007.05.012

Bramson, A. M., Byrne, S., & Bapst, J. (2017). Preservation of midlatitude ice sheets on Mars. *Journal of Geophysical Research: Planets*, *122*, 2250–2266. https://doi.org/10.1002/2017JE005357

Brothers, S. C., Kocurek, G., & Holt, J. W. (2018). Sequence architecture of the cavi unit, Chasma Boreale, Mars. *Icarus*, *308*, 42–60. https://doi.org/10.1016/j.icarus.2017.06.024

Brothers, T. C., Holt, J. W., & Spiga, A. (2015). Planum Boreum basal unit topography, Mars: Irregularities and insights from SHARAD. *Journal of Geophysical Research: Planets*, *120*, 1357–1375. https://doi.org/10.1002/2015JE004830

Brouet, Y., Neves, L., Sabouroux, P., Levasseur-Regourd, A. C., Poch, O., Encrenaz, P., et al. (2016). Characterization of the permittivity of controlled porous water ice-dust mixtures to support the radar exploration of icy bodies. *Journal of Geophysical Research: Planets*, *121*, 2426–2443. https://doi.org/10.1002/2016JE005045

Byrne, S. (2009). The polar deposits of Mars. *Annual Review of Earth and Planetary Sciences*, *37*(1), 535–560. https://doi.org/10.1146/annurev.earth.031208.100101

Byrne, S., & Murray, B. C. (2002). North polar stratigraphy and the paleo-erg of Mars. *Journal of Geophysical Research*, *107*(E6), 5044. https://doi.org/10.1029/2001JE001615

Calvin, W. M., Roach, L. H., Seelos, F. P., Seelos, K. D., Green, R. O., Murchie, S. L., & Mustard, J. F. (2009). Compact Reconnaissance Imaging Spectrometer for Mars observations of northern Martian latitudes in summer. *Journal of Geophysical Research*, 114, E00D11. https://doi.org/10.1029/2009JE003348

Campbell, B. A., Putzig, N. E., Carter, L. M., & Phillips, R. J. (2011). Autofocus correction of phase distortion effects on SHARAD echoes. *IEEE Geoscience and Remote Sensing Letters*, *8*(5), 939–942. https://doi.org/10.1109/LGRS.2011.2143692

Chevrier, V., Sears, D. W. G., Chittenden, J. D., Roe, L. A., Ulrich, R., Bryson, K., et al. (2007). Sublimation rate of ice under simulated Mars conditions and the effect of layers of mock regolith JSC Mars-1. *Geophysical Research Letters*, *34*, L02203. https://doi.org/10.1029/2006GL028401

Conway, S. J., Hovius, N., Barnie, T., Besserer, J., Le Mouélic, S., Orosei, R., & Read, N. A. (2012). Climate-driven deposition of water ice and the formation of mounds in craters in Mars' north polar region. *Icarus*, *220*(1), 174–193. https://doi.org/10.1016/j.icarus.2012.04.021

Dickinson, W. W., & Ward, J. D. (1994). Low depositional porosity in eolian sands and sandstones, Namib Desert. *Journal of Sedimentary Research*, *64*(2a), 226–232. https://doi.org/10.1306/D4267D66-2B26-11D7-8648000102C1865D

Edgett, K. S., Williams, R. M. E., Malin, M. C., Cantor, B. A., & Thomas, P. C. (2003). Mars landscape evolution: influence of stratigraphy on geomorphology in the north polar region. *Geomorphology*, *52*(3), 289–297. https://doi.org/10.1016/S0169-555X(02)00262-3

Ewing, R. C., Peyret, A.-P. B., Kocurek, G., & Bourke, M. (2010). Dune field pattern formation and recent transporting winds in the Olympia Undae Dune Field, north polar region of Mars. *Journal of Geophysical Research*, *115*, E08005. https://doi.org/10.1029/2009JE003526

Feldman, W., Bourke, M., Elphic, R., Maurice, S., Bandfield, J., Prettyman, T., et al. (2008). Hydrogen content of sand dunes within Olympia Undae. *Icarus*, *196*(2), 422–432. https://doi.org/10.1016/j.icarus.2007.08.044

Fishbaugh, K. E., & Head, J. W. (2005). Origin and characteristics of the Mars north polar basal unit and implications for polar geologic history. *Icarus*, *174*(2), 444–474. https://doi.org/10.1016/j.icarus.2004.06.021

Fishbaugh, K. E., Poulet, F., Chevrier, V., Langevin, Y., & Bibring, J.-P. (2007). On the origin of gypsum in the Mars north polar region. *Journal of Geophysical Research*, 112, E07002. https://doi.org/10.1029/2006JE002862

Greve, R., Grieger, B., & Stenzel, O. J. (2010). MAIC-2, a latitudinal model for the Martian surface temperature, atmospheric water transport and surface glaciation. *Planetary and Space Science*, *58*(6), 931–940. https://doi.org/10.1016/j.pss.2010.03.002

Grima, C., Kofman, W., Mouginot, J., Phillips, R. J., Hérique, A., Biccari, D., et al. (2009). North polar deposits of Mars: Extreme purity of the water ice. *Geophysical Research Letters*, *36*, L03203. https://doi.org/10.1029/2008GL036326

Heggy, E., Clifford, S. M., Cosmidis, J., Humeaux, A., Boisson, J., & Morris, R. V. (2008). Geoelectrical model of the Martian north polar layered deposits (vol. 39, p. 2471). Presented at the Lunar and Planetary Science Conference. Retrieved from http://adsabs.harvard.edu/abs/2008LPI....39.2471H

Heggy, E., Paillou, P., Ruffie, G., Malezieux, J. M., Costard, F., & Grandjean, G. (2001). On water detection in the Martian subsurface using sounding radar. *Icarus*, *154*(2), 244–257. https://doi.org/10.1006/icar.2001.6717

Herkenhoff, K. E., Byrne, S., Russell, P. S., Fishbaugh, K. E., & McEwen, A. S. (2007). Meter-scale morphology of the north polar region of Mars. *Science*, *317*(5845), 1711–1715. https://doi.org/10.1126/science.1143544

Horgan, B. H., Bell, J. F. III, Noe Dobrea, E. Z., Cloutis, E. A., Bailey, D. T., Craig, M. A., et al. (2009). Distribution of hydrated minerals in the north polar region of Mars. *Journal of Geophysical Research*, *114*, E11012. https://doi.org/10.1029/2008JE003187

Kolbuszewski, J., Nadolski, L., & Dydacki, Z. (1950). Porosity of wind-deposited sands. *Geological Magazine*, *87*(6), 433–435. https://doi.org/10.1017/S001675680007744X

Lalich, D. E., & Holt, J. W. (2016). New Martian climate constraints from radar reflectivity within the north polar layered deposits. *Geophysical Research Letters*, *44*, 657–664. https://doi.org/10.1002/2016GL071323

Langevin, Y., Poulet, F., Bibring, J.-P., & Gondet, B. (2005). Sulfates in the north polar region of mars detected by OMEGA/Mars Express. *Science*, *307*(5715), 1584–1586. https://doi.org/10.1126/science.1109091

Laskar, J., Correia, A. C. M., Gastineau, M., Joutel, F., Levrard, B., & Robutel, P. (2004). Long term evolution and chaotic diffusion of the insolation quantities of Mars. *Icarus*, *170*(2), 343–364. https://doi.org/10.1016/j.icarus.2004.04.005

Lauro, S. E., Mattei, E., Soldovieri, F., Pettinelli, E., Orosei, R., & Vannaroni, G. (2012). Dielectric constant estimation of the uppermost basal unit layer in the Martian Boreales Scopuli region. *Icarus*, *219*(1), 458–467. https://doi.org/10.1016/j.icarus.2012.03.011

Levrard, B., Forget, F., Montmessin, F., & Laskar, J. (2007). Recent formation and evolution of northern Martian polar layered deposits as inferred from a global climate model. *Journal of Geophysical Research*, *112*, E06012. https://doi.org/10.1029/2006JE002772

Levy, J. S., Fassett, C. I., Head, J. W., Schwartz, C., & Watters, J. L. (2014). Sequestered glacial ice contribution to the global Martian water budget: Geometric constraints on the volume of remnant, midlatitude debris-covered glaciers. *Journal of Geophysical Research: Planets*, *119*, 2188–2196. https://doi.org/10.1002/2014JE004685

Malin, M. C., & Edgett, K. S. (2001). Mars Global Surveyor Mars Orbiter Camera: Interplanetary cruise through primary mission. *Journal of Geophysical Research*, *106*(E10), 23429–23570. https://doi.org/10.1029/2000JE001455

Massé, M., Bourgeois, O., Le Mouélic, S., Verpoorter, C., Le Deit, L., & Bibring, J. P. (2010). Martian polar and circum-polar sulfate-bearing deposits: Sublimation tills derived from the North Polar Cap. *Icarus*, *209*(2), 434–451. https://doi.org/10.1016/j.icarus.2010.04.017

Massé, M., Bourgeois, O., Le Mouélic, S., Verpoorter, C., Spiga, A., & Le Deit, L. (2012). Wide distribution and glacial origin of polar gypsum on Mars. *Earth and Planetary Science Letters*, *317*, 44–55. https://doi.org/10.1016/j.epsl.2011.11.035

Mattei, E., Lauro, S. E., Vannaroni, G., Cosciotti, B., Bella, F., & Pettinelli, E. (2014). Dielectric measurements and radar attenuation estimation of ice/basalt sand mixtures as Martian polar caps analogues. *Icarus*, *229*, 428–433. https://doi.org/10.1016/j.icarus.2013.10.017

Nerozzi, S., & Holt, J. W. (2017). Newly mapped extent, morphology, and internal stratigraphy of the Martian north polar cavi unit (Vol. 48, p. 1722). Presented at the Lunar and Planetary Science Conference. Retrieved from http://adsabs.harvard.edu/abs/2017LPI....48.1722N

Nerozzi, S., & Holt, J. W. (2018). Earliest accumulation history of the north polar layered deposits, Mars from SHARAD. *Icarus*, *308*, 128–137. https://doi.org/10.1016/j.icarus.2017.05.027

Nunes, D. C., & Phillips, R. J. (2006). Radar subsurface mapping of the polar layered deposits on Mars. *Journal of Geophysical Research*, *111*(E6), E06S21. https://doi.org/10.1029/2005JE002609

Ojha, L., Nerozzi, S., & Lewis, K. (2019). Compositional Constraints on the North Polar Cap of Mars from Gravity and Topography. *Geophysical Research Letters*. https://doi.org.10.1029/2019gl082294

Phillips, R. J., Zuber, M. T., Smrekar, S. E., Mellon, M. T., Head, J. W., Tanaka, K. L., et al. (2008). Mars north polar deposits: Stratigraphy, age, and geodynamical response. *Science*, *320*(5880), 1182–1185. https://doi.org/10.1126/science.1157546

Putzig, N. E., Mellon, M. T., Herkenhoff, K. E., Phillips, R. J., Davis, B. J., Ewer, K. J., & Bowers, L. M. (2014). Thermal behavior and ice-table depth within the north polar erg of Mars. *Icarus*, *230*, 64–76. https://doi.org/10.1016/j.icarus.2013.07.010

Putzig, N. E., Phillips, R. J., Campbell, B. A., Holt, J. W., Plaut, J. J., Carter, L. M., et al. (2009). Subsurface structure of Planum Boreum from Mars Reconnaissance Orbiter Shallow Radar soundings. *Icarus*, *204*(2), 443–457. https://doi.org/10.1016/j.icarus.2009.07.034

Pye, K., & Tsoar, H. (1990). *Aeolian sand and sand dunes*. Netherlands. Retrieved from: Springer. www.springer.com/us/book/9789401159883

Roach, L. H., Mustard, J. F., Murchie, S., Langevin, Y., Bibring, J.-P., Bishop, J., et al., & CRISM Team (2007). CRISM spectral signatures of the north polar gypsum dunes (Vol. *38*, p. 1970). Presented at the Lunar and Planetary Science Conference. Retrieved from http://adsabs.harvard.edu/abs/2007LPI....38.1970R

Schatz, V., Tsoar, H., Edgett, K. S., Parteli, E. J. R., & Herrmann, H. J. (2006). Evidence for indurated sand dunes in the Martian north polar region. *Journal of Geophysical Research*, *111*, E04006. https://doi.org/10.1029/2005JE002514

Selvans, M. M., Plaut, J. J., Aharonson, O., & Safaeinili, A. (2010). Internal structure of Planum Boreum, from Mars advanced radar for subsurface and ionospheric sounding data. *Journal of Geophysical Research*, *115*, E09003. https://doi.org/10.1029/2009JE003537

Seu, R., Biccari, D., Orosei, R., Lorenzoni, L. V., Phillips, R. J., Marinangeli, L., et al. (2004). SHARAD: The MRO 2005 shallow radar. *Planetary and Space Science*, *52*(1-3), 157–166. https://doi.org/10.1016/j.pss.2003.08.024

Seu, R., Phillips, R. J., Biccari, D., Orosei, R., Masdea, A., Picardi, G., et al. (2007). SHARAD sounding radar on the Mars Reconnaissance Orbiter. *Journal of Geophysical Research*, *112*, E05S05. https://doi.org/10.1029/2006JE002745

Skinner, J. A., & Herkenhoff, K. E. (2012). Geologic map of the MTM 85200 Quadrangle, Olympia Rupes Region of Mars. Retrieved July 30, 2018, from https://pubs.usgs.gov/sim/3197/

Skorov, Y. V., Markiewicz, W. J., Basilevsky, A. T., & Keller, H. U. (2001). Stability of water ice under a porous nonvolatile layer: Implications to the south polar layered deposits of Mars. *Planetary and Space Science*, *49*(1), 59–63. https://doi.org/10.1016/S0032-0633(00)00121-5

Stillman, D. E., Grimm, R. E., & Dec, S. F. (2010). Low-frequency electrical properties of ice−silicate mixtures. *The Journal of Physical Chemistry B*, *114*(18), 6065–6073. https://doi.org/10.1021/jp9070778

Tanaka, K., Rodriguez, J., Skinner, J. Jr., Bourke, M., Fortezzo, C., Herkenhoff, K., et al. (2008). North polar region of Mars: Advances in stratigraphy, structure, and erosional modification. *Icarus*, *196*(2), 318–358. https://doi.org/10.1016/j.icarus.2008.01.021

Tanaka, K. L., & Fortezzo, C. M. (2012). Geologic map of the north polar region of Mars. Retrieved March 17, 2017, from https://pubs.usgs.gov/sim/3177/

Williams, K. E., Toon, O. B., Heldmann, J. L., McKay, C., & Mellon, M. T. (2008). Stability of mid-latitude snowpacks on Mars. *Icarus*, *196*(2), 565–577. https://doi.org/10.1016/j.icarus.2008.03.017

Zuber, M. T., Smith, D. E., Solomon, S. C., Abshire, J. B., Afzal, R. S., Aharonson, O., et al. (1998). Observations of the North Polar Region of Mars from the Mars Orbiter Laser Altimeter. *Science*, *282*(5396), 2053–2060. https://doi.org/10.1126/science.282.5396.2053